Zhang *et al. Microstructures* **2025**, *5*, 2025005
DOI: 10.20517/microstructures.2024.81

Microstructures

Research Article

Open Access

Check for updates

Thermoelectric transport properties of $BaFe_2Fe_{16}O_{27}$ hexaferrites

Xiaozhi Zhang[1], Ling Fu[2], Zhenyu Pan[2], Shun Wan[3], Tian-Ran Wei[2]

[1]Department of Physics, College of Sciences, Shanghai University, Shanghai 200444, China.
[2]State Key Laboratory of Metal Matrix Composites, School of Materials Science and Engineering, Shanghai Jiao Tong University, Shanghai 200240, China.
[3]Wuzhen Laboratory, Tongxiang 314500, Zhejiang, China.

Correspondence to: Dr. Zhenyu Pan, State Key Laboratory of Metal Matrix Composites, School of Materials Science and Engineering, Shanghai Jiao Tong University, 800 Dongchuan Road, Minhang District, Shanghai 200240, China. E-mail: zpan@sjtu.edu.cn; Dr. Shun Wan, Wuzhen Laboratory, No. 925 Daole Road, Tongxiang 314500, Zhejiang, China. E-mail: wans@wuzhenlab.com

How to cite this article: Zhang, X.; Fu, L.; Pan, Z.; Wan, S.; Wei, T. R. Thermoelectric transport properties of $BaFe_2Fe_{16}O_{27}$ hexaferrites. *Microstructures* **2025**, *5*, 2025005. https://dx.doi.org/10.20517/microstructures.2024.81

Received: 30 Aug 2024 **First Decision:** 14 Oct 2024 **Revised:** 7 Nov 2024 **Accepted:** 19 Nov 2024 **Published:** 22 Jan 2025

Academic Editors: Rongkun Zheng, Jing-Feng Li **Copy Editor:** Fangling Lan **Production Editor:** Fangling Lan

Abstract

Exploring new materials with earth-abundant and low-toxicity elements has been a long-standing goal in thermoelectrics. Hexaferrites, a family of environmentally friendly oxides, exhibit complex and tunable structures and excellent magnetic properties, but receive limited attention as potential thermoelectric materials. Here in this study, we systematically investigated the thermoelectric transport properties of W-type hexaferrites $BaFe_2Fe_{16}O_{27}$ and the cobalt-substituted derivatives prepared by sintering in the nitrogen atmosphere. These materials exhibit an n-type conduction behavior and cobalt substitution can tune the electrical transport properties effectively. Low-temperature specific heat capacity analysis unravels the existence of low-energy optical phonons that contribute to damping the heat transport. Low room temperature thermal conductivity of 1.27 W m^{-1} K^{-1} is obtained, and the role of cobalt substitution on the thermal conductivity reduction is rationalized by the Debye-Callaway model. This study enlightens the investigation of the thermoelectric transport properties of W-type hexaferrites $BaFe_2Fe_{16}O_{27}$ and extends the scope of new thermoelectric compounds.

Keywords: Oxide thermoelectric materials, hexaferrite, $BaFe_2Fe_{16}O_{27}$, thermal conductivity

© The Author(s) 2025. **Open Access** This article is licensed under a Creative Commons Attribution 4.0 International License (https://creativecommons.org/licenses/by/4.0/), which permits unrestricted use, sharing, adaptation, distribution and reproduction in any medium or format, for any purpose, even commercially, as long as you give appropriate credit to the original author(s) and the source, provide a link to the Creative Commons license, and indicate if changes were made.

INTRODUCTION

Over the past decades, developing thermoelectric technology to directly convert energy between heat and electricity has drawn significant attention[1,2]. The dimensionless figure of merit (zT) of thermoelectric material is a vital parameter to determine the maximum conversion efficiency, which is defined as $zT = S^2\sigma T/\kappa$, where S, σ, T, and κ are the Seebeck coefficient, electrical conductivity, absolute temperature, and thermal conductivity, respectively[3]. A high zT value usually achieves high conversion efficiency, so decoupling the interrelation between the electrical transport parameters S, σ and thermal transport parameter κ has been the key task for thermoelectric research[4-7]. Moreover, exploring new thermoelectric materials with eco-friendly and earth-abundant elements is economically and sustainably essential to large-scale production and commercial applications[8-10].

Oxide ceramics have been widely studied as promising thermoelectric materials by virtue of low cost, low toxicity, good stability, and simple preparation methods[11,12]. Starting from the single-crystalline $Na_xCoO_{2-\delta}$ in 2001[13], several promising thermoelectric oxides, such as $Ca_3Co_4O_9$[14], In_2O_3[15], and $SrTiO_3$[16], have been discovered or developed. Particularly, in the early 2010s, the layered compound BiCuSeO with an inherent "phonon glass, electron crystal" has been found to show exceptional thermoelectric performance, reaching a maximum zT of around 1.4[17,18]. Therefore, complex-structured materials are considered potential thermoelectric candidates. However, considering the vast number of oxide materials, the transport properties and thermoelectric performance are still to be studied for a variety of materials.

Hexaferrites, a large family of multinary iron oxides, have attracted great attention for various applications such as magnetic recording, electromagnetic wave control, and communication equipment manufacture[19-22]. They exhibit superior magneto-crystalline anisotropy, good chemical stability and low cost[23-25]. In recent years, hexaferrites have also been found to possess new properties such as multiferroicity and low-field magnetoelectric effects at room temperature, making them a popular material system in condensed matter physics[26,27]. According to their building blocks and the stacking order, there are six types of hexaferrites including W-type, M-type, X-type, Y-type, Z-type, and U-type ferrites[25]. As to the electrical and thermal transport properties, all types of hexaferrites adopt a large and complex unit cell, which is likely to give rise to abundant optical phonons damping heat transport[28]. Among them, W-type hexaferrites $BaMe_2Fe_{16}O_{27}$ (abbreviated as Me_2W, where Me denotes a divalent metal) are particularly interesting for thermoelectrics since they exhibit relatively high and tuneable electrical conductivity by virtue of the coexistence of Me^{2+} and Fe^{3+}[29-31]. However, little knowledge is available regarding the thermal transport properties, which are important not only to thermoelectrics but also to thermal management in electromagnetic applications.

The synthesis, transport properties, and thermoelectric performance of a series of W-type hexaferrites $BaFe_{2-x}Co_xFe_{16}O_{27}$ (abbreviated as $Fe_{2-x}Co_xW$) are reported in this study. Polycrystalline materials with high phase purity and crystallinity are successfully synthesized via a solid-state reaction in a nitrogen atmosphere. Electrical and thermal transport properties are comprehensively studied combining both experiments and modeling. Low κ values are achieved by Co substitution and the thermal transport properties are well modeled. This work largely enriches the knowledge on the thermoelectric transport physics and mechanisms of hexaferrites.

MATERIALS AND METHOD

A solid-state reaction method was used to synthesize pristine and cobalt-substituted W-type hexaferrites with nominal compositions of $BaFe_{2-x}Co_xFe_{16}O_{27}$ (x = 0, 0.2, 0.4, 1). $BaCO_3$, Fe_2O_3 and Co_3O_4 powders of analytical purity were used as the raw materials and mixed well after being weighted according to formula.

Then, the mixture was first subjected to high-temperature calcination of 1,200 °C for 20 h in a tube furnace in a flowing nitrogen atmosphere. The resulting materials were ground into fine powders by using a mortar and pestle after calcination, followed by adding a self-prepared 5 wt% polyvinyl alcohol (PVA) solution as an adhesive for the granulation process. Finally, the granulated powder was compacted into disk-shaped pellets and preheated at 600 °C for 1.5 h in the air to expel the PVA, followed by another sintering process in nitrogen at 1,240 °C for 4 h to obtain the $BaFe_{2-x}Co_xFe_{16}O_{27}$ (x = 0, 0.2, 0.4, 1.0) ceramics.

Powder X-ray diffraction (XRD, Bruker D8 Advance) was employed to determine the phases of all materials. A scanning electron microscope (SEM, ZEISS Sigma300) was used to examine surface microstructures. The σ and S were measured ranging from 300 to 1,000 K under a helium atmosphere by ZEM-3 (ULVAC-RIKO) apparatus. The κ was calculated according to $\kappa = d\lambda C_p$. Here, the density d and the thermal diffusivity λ were measured by the Archimedes method and laser flash method (LFA-457, Netzsch), respectively. Additionally, Dulong-Petit law was used to estimate the specific heat capacity C_p. Physical Property Measurement System (PPMS, Quantum Design) was employed to measure the low-temperature heat capacity. Raman measurements were conducted by a Raman spectrometer using a 633 nm laser (HORIBA Scientific). Measurement uncertainties for S, σ, and κ are around 5%, 5% and 7%, respectively[5].

Vienna Ab initio Simulation Package (VASP) was used to perform the density functional theory (DFT) calculations[32]. The generalized gradient approximation (GGA) parameterized by Perdew, Burke and Ernzerhof (PBE) was used for the exchange-correlation terms[33]. The $5s^25p^66s^2$, $3d^74s^1$, and $2s^22p^4$ electrons were treated as valence electrons in the projector-augmented wave (PAW) potentials for Ba, Fe and O, respectively[34]. All GGA + U calculations used Dudarev's approximation with U equivalent to the U_{eff} parameter ($U_{eff} = U - J$, where U and J represent Hubbard on-site Coulomb energy and the exchange parameter, respectively)[35]. An energy cutoff of 600 eV for the plane waves was adopted and reciprocal space was sampled on G-centered k-point grids with a resolution of 0.03 π/Å, with convergence thresholds of 1×10^{-6} eV for electronic energy and 1×10^{-2} eV/Å for force. U = 4 eV was used for Fe 3d orbital in all GGA + U calculations. All calculations were spin-polarized with atomic spin configurations initialized according to the Gorter scheme. Elastic constants were determined according to the energy-strain method and the elastic tensor was processed using the Voigt-Reuss-Hill approximation[36]. Visualization for Electronic and Structural Analysis (VESTA) software was used to model the structures of the material[37] and visualize the charge densities and the electron localized function (ELF).

RESULTS AND DISCUSSION

XRD and microstructure analysis

Figure 1A shows the hexagonal crystal structure of $BaFe_2Fe_{16}O_{27}$ material (space group $P6_3/mmc$). Blocks of R $(BaFe_6O_{11})^{2-}$ and S $(Fe_6O_8)^{2+}$ are usually used to describe the crystal structure of the W-type hexaferrite $BaFe_2Fe_{16}O_{27}$, and the stacking arrangement of the material is RSSR*S*S*, where the asterisk indicates a specific block rotated 180° around the c axis[38-40]. As presented in Figure 1A and Supplementary Figure 1, the calculated Bader charge of Fe ions in $BaFe_2Fe_{16}O_{27}$ ranges between +1.44 and +1.76. This is slightly lower than the values in literature reported before[41]. The Bader charge for Ba is +1.58, while the value for O is in a range of (-1.0~-1.21), similar to the reported charge value of -1.16 for O atomic calculated in water molecular[42]. Supplementary Figure 1A presents the calculated electron localization function (ELF) and charge density of $BaFe_2Fe_{16}O_{27}$. It is clearly seen that electrons from the Ba and Fe are transferred to the nearby oxygen, a typical characteristic of the ionic material.

Room-temperature XRD patterns of all $BaFe_{2-x}Co_xFe_{16}O_{27}$ (x = 0, 0.2, 0.4, 1.0) hexaferrites are presented in Figure 1B. All the diffraction peaks can be indexed to the standard $BaFe_{18}O_{27}$ compound, and no secondary

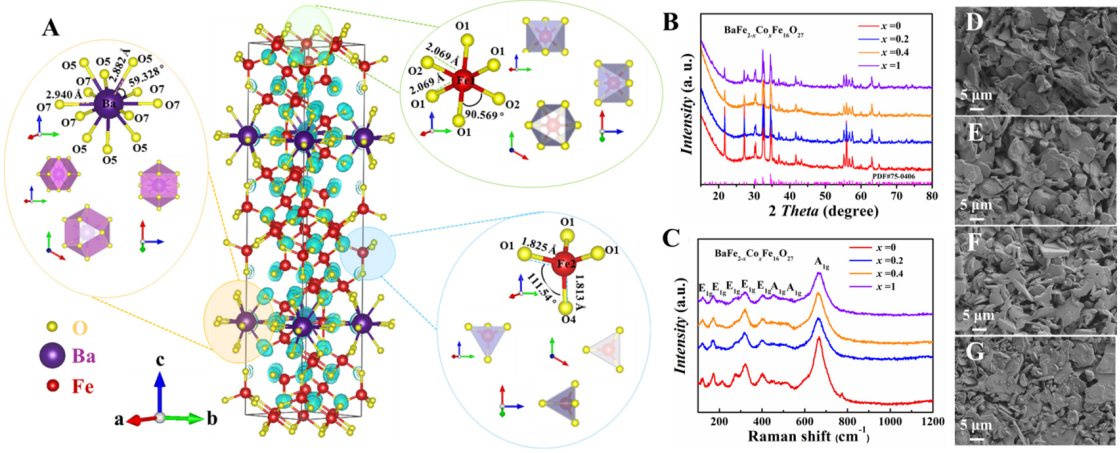

Figure 1. (A) Crystal structure of $BaFe_2Fe_{16}O_{27}$. The local bonding of Ba and Fe (at 6g and 4e sites) ions are highlighted. (B) Powder XRD patterns of $BaFe_{2-x}Co_xFe_{16}O_{27}$ (x = 0, 0.2, 0.4, 1.0) hexaferrites. (C) Raman spectra and (D-G) SEM surface images of $BaFe_{2-x}Co_xFe_{16}O_{27}$.

phases are observed. The Co substitution does not cause an obvious shift in the XRD peak positions, likely due to the similar ionic radii between Co^{2+} (~0.82 Å) and Fe^{2+} (~0.83 Å). As displayed in Figure 1C, the dominant Raman peaks of all $BaFe_{2-x}Co_xFe_{16}O_{27}$ (x = 0, 0.2, 0.4, 1.0) hexaferrites are located at 124, 174, 213, 276, 321, 463, 514 and 670 cm^{-1}, relating to the intrinsic vibrations of hexagonal hexaferrite crystal[43]. Lamellar grains are observed by SEM [Figure 1D-G], consistent with the hexagonal layered structure. Noticeably, micro-sized pores are found, resulting in a low relative density of 64.7%~73.2%.

Electrical transport properties

Considering the cases of both spin up and spin down for Fe ions, we calculated the electronic band structures of $BaFe_2Fe_{16}O_{27}$. As displayed in Figure 2A and B, the conduction-band minimum and valence-band maximum are located on the Γ and H points, respectively. Along the direction parallel to the c-axis, eigenenergy dispersion curves change slowly, while curves perpendicular to the c-axis are steep, indicating a larger effective mass of carriers along the c-axis, which aligns well with expectations for layered materials. The computed total density of state (TDOS) presented in Figure 2C for $BaFe_2Fe_{16}O_{27}$ shows a small band gap of ~ 0.17 eV. Besides, the calculated high symmetry points of $BaFe_2Fe_{16}O_{27}$ are presented in Figure 2D.

Figure 3A and B presents the temperature-dependent σ and S for all $BaFe_{2-x}Co_xFe_{16}O_{27}$ (x = 0, 0.2, 0.4, 1.0) hexaferrites from 300 to 1,000 K. For all the samples, the σ values are around 10^1-10^2 S m^{-1} at 300 K and increase with temperature, exhibiting a non-degenerate semiconductor behavior. Below ~900 K, Co-doped samples show relatively lower σ values compared with the pristine ones. In the whole temperature range, all S values are negative, indicating an n-type conduction behavior. In line with the composition-dependence of electrical conductivity, the alloyed samples exhibit higher S values than the undoped ones. This suggests that Co substitution probably decreases the carrier concentration. Moreover, according to a previous study[41], valence states of 6g sites can be changed from mixed valence state to 3+ by Co doping. Therefore, the energy of Fe will increase and enter into the conduction band, leading to the disappearance of "heavily doping states" and thus the decrease of the carrier concentration and electrical conductivity. For $BaFe_1Co_1Fe_{16}O_{27}$, the sudden decrease of S with T around 800 K suggests a phase transition. This phase transition may be a magnetic phase transition caused by magnetic moment arrangement changes originating from the change of lattice parameters at high temperatures[25,44]. Maximum power factors (PFs) reach 0.26 μW cm^{-1} K^{-2} for Fe_1Co_1W at 1,000 K [Figure 3C]. As shown in Figure 3D, the S and σ roughly follow the single parabolic band (SPB) model[45].

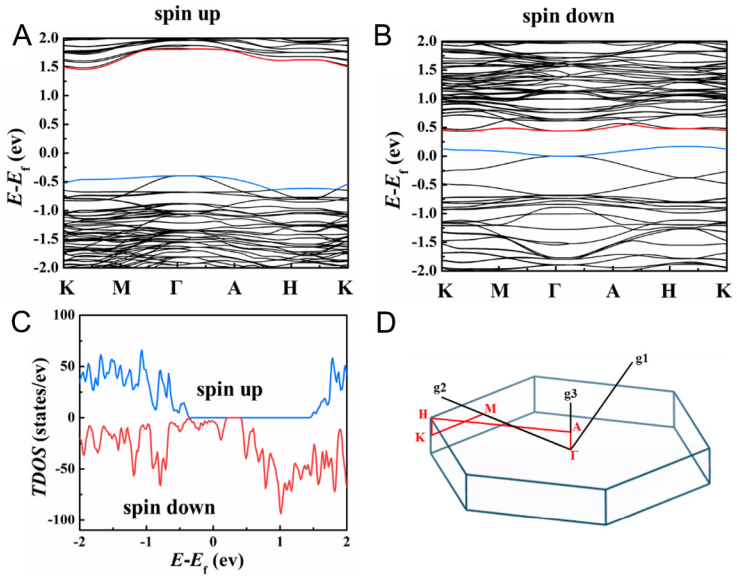

Figure 2. (A) Spin up and (B) Spin down energy band structures along the high symmetry directions. (C) Total density of states of $BaFe_2Fe_{16}O_{27}$. (D) Calculated high symmetry points of $BaFe_2Fe_{16}O_{27}$.

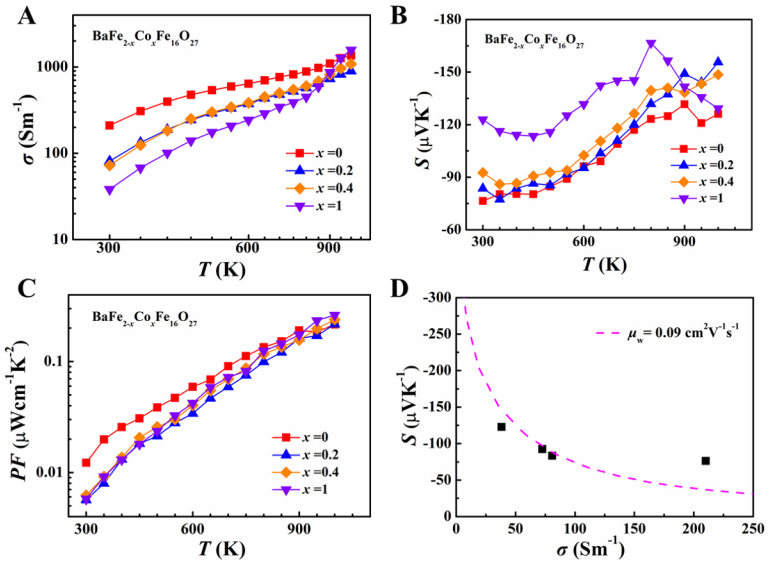

Figure 3. Temperature-dependent (A) σ, (B) S, and (C) PF between 300 and 1,000 K for $BaFe_{2-x}Co_xFe_{16}O_{27}$. (D) Room-temperature S *vs.* σ plot. The dashed line is fitted based on SPB model using a fixed weighted mobility.

ELASTIC AND THERMAL PROPERTIES

We carried out the DFT calculation to obtain the elastic parameters of pristine $BaFe_2Fe_{16}O_{27}$. As shown in Table 1, the average sound speed and the Debye temperature θ_D calculated are 3,667 m/s and 517 K, respectively. The values are higher than common thermoelectric materials, reflecting the stiffer bonding of $BaFe_2Fe_{16}O_{27}$ [46,47]. The low-temperature heat capacity was measured and modeled for further understanding of the lattice dynamics. One Debye mode and two Einstein modes are needed to accurately describe the data, as presented in Figure 4[48,49]. The fitted Debye temperature is 516 K [Supplementary Table 1], which is in excellent consistency with the DFT calculation above (517 K). The Einstein temperatures are fitted to be

Table 1. DFT-calculated elastic and physical properties of $BaFe_2Fe_{16}O_{27}$

Elastic parameters	Calculated value
C_{11} (GPa)	321
C_{12} (GPa)	190
C_{13} (GPa)	182
C_{33} (GPa)	301
C_{44} (GPa)	61.9
C_{66} (GPa)	65.6
Bulk modulus B (GPa)	228
Young's modulus E (GPa)	175
Shear modulus G (GPa)	63.8
Poisson's ratio v	0.372
Pugh's ratio (B/G)	3.57
Longitudinal wave velocity (m/s)	7,204
Transverse wave velocity (m/s)	3,252
Average wave velocity (m/s)	3,667
Debye temperature (K)	517

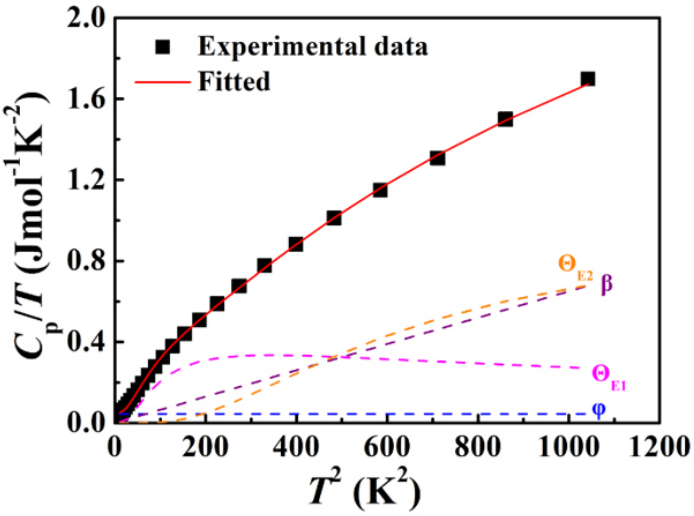

Figure 4. C_p/T as a function of T^2 for $BaFe_2Fe_{16}O_{27}$ at low temperature. Black squares represent the experimental data. The red solid line represents the fitted curve by using one Debye mode and two Einstein modes. The other dashed lines represent the electronic term φ, Debye term β, and two Einstein terms, Θ_{E1} and Θ_{E2}, respectively. The adjusted R^2 value for the fitted curve is 0.99959 and the Chi-squared value is 6.058×10^{-3}.

47.7 and 127 K, corresponding to the phonon energies of 4.1 and 11 meV, respectively. The low-energy optical phonons are also consistent with the Raman measurement mentioned above (peak around 124 cm^{-1}, aka 15.4 meV), which should damp part of the heat transport.

Figure 5A shows the temperature-dependent κ for all $BaFe_{2-x}Co_xFe_{16}O_{27}$ samples. Considering the low σ, the electronic portion of κ contributes as low as 1%-3% at 300 K, so the lattice thermal conductivity (κ_L) can be treated numerically equal to the total one. Low κ values of 1.27 W m^{-1} K^{-1} at 300 K and 0.69 W m^{-1} K^{-1} at 750 K are obtained in the $Fe_{1.8}Co_{0.2}W$ sample. The room-temperature κ values are pretty low among oxides compared to other counterparts such as $In_{1.99}Ge_{0.01}O_3$ (11.5 W m^{-1} K^{-1})[15], $SrTiO_3$ (8.1 W m^{-1} K^{-1})[50] and $Ca_3Co_4O_9$ ceramic (2.3 W m^{-1} K^{-1})[51]. Nonetheless, the values may not reflect the intrinsic properties of the

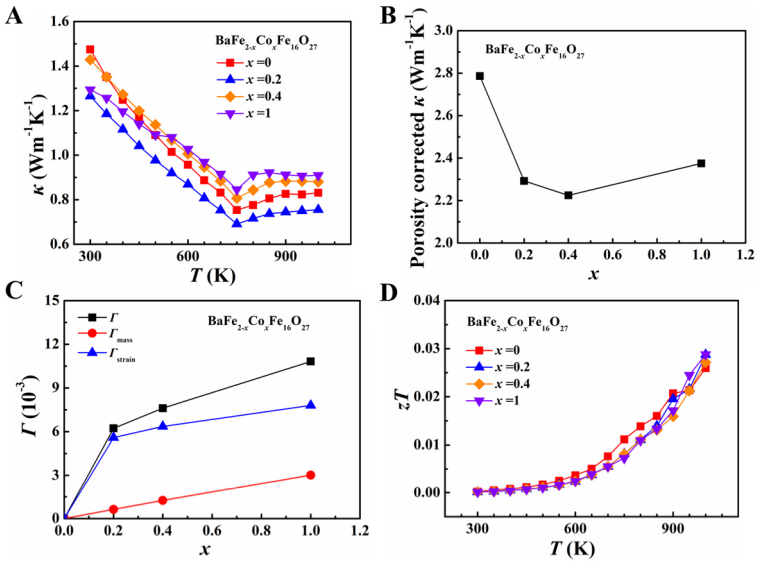

Figure 5. (A) Thermal conductivity (κ) varying with temperature for $BaFe_{2-x}Co_xFe_{16}O_{27}$ hexaferrites. (B) Porosity-corrected thermal conductivities as functions of content of Co for $BaFe_{2-x}Co_xFe_{16}O_{27}$ at 300 K. (C) Point-defect scattering parameter Γ, Γ_{mass} and Γ_{strain} as a function of Co content. (D) zT varying with temperature.

samples since there exists an appreciable number of pores. Therefore, for further analysis, we correct the thermal conductivity values by the porosity via[52]

$$\frac{\kappa_{real}}{\kappa_{dense}} = 1 - \frac{4}{3}\Phi \quad (1)$$

where κ_{real} is the measured thermal conductivity, κ_{dense} corresponds to that of fully dense samples, and Φ is the porosity. The corrected thermal conductivities as a function of Co content at room temperature are shown in Figure 5B. Apparently, the existing pores can lead to the decrease of the thermal conductivity but their influence on the thermoelectric performance can be complicated as they will also lower the carrier mobility, thus reducing electrical conductivity. There is a ~20% reduction of κ when x increases from 0 to 0.4. This reduction is mainly attributed to the point defect scattering induced by Co substitution for Fe. Based on the fitted results within the Debye-Callaway framework, we derive the point-defect scattering parameter Γ, which includes mass fluctuation (Γ_{mass}) and strain field fluctuation (Γ_{strain})[53]. The fitted results of temperature-dependent thermal conductivity are presented in Supplementary Figure 2. As plotted in Figure 5C, Γ_{strain} dominates the point-defect scattering. This is reasonable since the mass difference between Co and Fe is less than 6%, so the contributions of Γ_{mass} should be small.

Figure 5D presents the zT for all $BaFe_{2-x}Co_xFe_{16}O_{27}$ (x = 0, 0.2, 0.4, 1.0) samples calculated based on the measured transport properties. The reduced thermal conductivity compensates for the deterioration in electrical properties, resulting in a similar calculated zT in all $BaFe_{2-x}Co_xFe_{16}O_{27}$ samples. Maximum zT around 0.03 at 1,000 K is achieved for all $BaFe_{2-x}Co_xFe_{16}O_{27}$ samples. Further optimizing the electrical transport properties may push zT to higher values.

CONCLUSIONS

In summary, thermoelectric transport properties of polycrystalline $BaFe_{2-x}Co_xFe_{16}O_{27}$ (x = 0, 0.2, 0.4, 1.0) hexaferrites have been systematically investigated. The DFT calculations indicate a band gap of around

0.17 eV and a strong anisotropy in band structure. The materials exhibit an n-type conduction behavior and Co substitution can tune the electrical transport properties effectively. Low κ values of 1.27 W m^{-1} K^{-1} at 300 K and 0.69 $Wm^{-1}K^{-1}$ at 750 K have been achieved in the $Fe_{1.8}Co_{0.2}W$ sample. The low thermal conductivity can be ascribed to point-defect scattering, the low-energy optical phonons, and the pores formed during synthesis. This work enriches the knowledge on the thermoelectric properties of hexaferrites.

DECLARATIONS

Authors' contributions

Conceptualization, writing-reviewing and editing: Pan, Z.; Wan, S.; Wei, T. R.
Methodology, software, writing-original draft: Zhang, X.
Formal analysis: Zhang, X.; Fu, L.; Pan, Z.; Wan, S.
Investigations, data curation: Zhang, X.; Fu, L.; Wan, S.
Supervision, resources, funding acquisition: Wan, S.; Wei, T. R.

Availability of data and materials

The data that support the findings of this study are available from the corresponding author upon reasonable request.

Financial support and sponsorship

The work is supported by Shanghai Post-doctoral Excellence Program and the Wuzhen Laboratory (WZLTD210603).

Conflicts of interest

All authors declared that there are no conflicts of interest.

Ethical approval and consent to participate

Not applicable.

Consent for publication

Not applicable.

Copyright

© The Author(s) 2025.

REFERENCES

1. He, J.; Tritt, T. M. Advances in thermoelectric materials research: looking back and moving forward. *Science* **2017**, *357*, eaak9997. DOI PubMed
2. Snyder, G. J.; Toberer, E. S. Complex thermoelectric materials. *Nat. Mater.* **2008**, *7*, 105-14. DOI PubMed
3. Yang, J.; Shi, X.; Zhang, W.; Chen, L.; Yang, J. Ab initio-based band engineering and rational design of thermoelectric materials. In: Materials, preparation, and characterization in thermoelectrics. New York: CRC press. 2012. DOI
4. Lin, S.; Guo, L.; Wang, X.; et al. Revealing the promising near-room-temperature thermoelectric performance in Ag_2Se single crystals. *J. Mater.* **2023**, *9*, 754-61. DOI
5. Wei, T. R.; Guan, M.; Yu, J.; Zhu, T.; Chen, L.; Shi, X. How to measure thermoelectric properties reliably. *Joule* **2018**, *2*, 2183-8. DOI
6. Tan, G.; Zhao, L. D.; Kanatzidis, M. G. Rationally designing high-performance bulk thermoelectric materials. *Chem. Rev.* **2016**, *116*, 12123-49. DOI PubMed
7. Zhu, T.; Liu, Y.; Fu, C.; Heremans, J. P.; Snyder, J. G.; Zhao, X. Compromise and synergy in high-efficiency thermoelectric materials. *Adv. Mater.* **2017**, *29*, 1605884. DOI
8. Liu, W. D.; Chen, Z. G.; Zou, J. Eco-friendly higher manganese silicide thermoelectric materials: progress and future challenges. *Adv. Energy. Mater.* **2018**, *8*, 1800056. DOI
9. Lu, X.; Morelli, D. T.; Xia, Y.; et al. High performance thermoelectricity in earth-abundant compounds based on natural mineral

tetrahedrites. *Adv. Energy. Mater.* **2013**, *3*, 342-8. DOI

10. Wei, T. R.; Qiu, P.; Zhao, K.; Shi, X.; Chen, L. Ag_2Q-based (Q = S, Se, Te) silver chalcogenide thermoelectric materials. *Adv. Mater.* **2023**, *35*, e2110236. DOI
11. Liu, Y.; Zhi, J.; Li, W.; Yang, Q.; Zhang, L.; Zhang, Y. Oxide materials for thermoelectric conversion. *Molecules* **2023**, *28*, 5894. DOI PubMed PMC
12. Zhao, Z.; Zhang, X.; Zhao, L. D. Strategies for manipulating thermoelectric properties of layered oxides. *Matter* **2023**, *6*, 3274-95. DOI
13. Terasaki, I.; Sasago, Y.; Uchinokura, K. Large thermoelectric power in $NaCo_2O_4$ single crystals. *Phys. Rev. B.* **1997**, *56*, R12685. DOI
14. Van Nong N, Pryds N, Linderoth S, Ohtaki M. Enhancement of the thermoelectric performance of p-type layered oxide $Ca_3Co_4O_{9+\delta}$ through heavy doping and metallic nanoinclusions. *Adv. Mater.* **2011**, *23*, 2484-90. DOI PubMed
15. Combe, E.; Guilmeau, E.; Savary, E.; et al. Microwave sintering of Ge-doped In_2O_3 thermoelectric ceramics prepared by slip casting process. *J. Eur. Ceram. Soc.* **2015**, *35*, 145-51. DOI
16. Li, Y.; Liu, X.; Zhang, P.; Han, Y.; Huang, M.; Wan, C. Theoretical insights into the Peierls plasticity in $SrTiO_3$ ceramics via dislocation remodelling. *Nat. Commun.* **2022**, *13*, 6925. DOI PubMed PMC
17. Zhao, L. D.; He, J.; Berardan, D.; et al. BiCuSeO oxyselenides: new promising thermoelectric materials. *Energy. Environ. Sci.* **2014**, *7*, 2900-24. DOI
18. Li, F.; Li, J. F.; Zhao, L. D.; et al. Polycrystalline BiCuSeO oxide as a potential thermoelectric material. *Energy. Environ. Sci.* **2012**, *5*, 7188-95. DOI
19. Li, Q.; Chen, Y.; Yu, C.; Young, L.; Spector, J.; Harris, V. G. Emerging magnetodielectric materials for 5G communications: 18H hexaferrites. *Acta. Mater.* **2022**, *231*, 117854. DOI
20. Jasrotia, R.; Prakash, J.; Himanshi; et al. Advancements in doping strategies for enhancing applications of M-type hexaferrites: a comprehensive review. *Prog. Solid. State. Chem.* **2023**, *72*, 100427. DOI
21. Hu, C.; Jiang, T.; Qian, Q.; Liu, C.; Wu, F.; Ji, G. Rare earth Nd^{3+} ions-doped W-type barium ferrite for efficient microwave absorption and its optimization mechanism. *J. Mater. Sci. Mater. Electron.* **2023**, *34*, 2295. DOI
22. Shan, S.; Li, J.; Zhao, X.; et al. Magnetic properties of Sm-doped M-type barium ferrite by high-energy ball mill-assisted solid-phase reaction method. *J. Magn. Magn. Mater.* **2024**, *589*, 171558. DOI
23. Jasrotia, R.; Pratap, S. V.; Kumar, R.; Singha, K.; Chandel, M.; Singh, M. Analysis of Cd^{2+} and In^{3+} ions doping on microstructure, optical, magnetic and mossbauer spectral properties of sol-gel synthesized BaM hexagonal ferrite based nanomaterials. *Res. Phy.* **2019**, *12*, 1933-41. DOI
24. Nikmanesh, H.; Hoghoghifard, S.; Hadi-Sichani, B. Study of the structural, magnetic, and microwave absorption properties of the simultaneous substitution of several cations in the barium hexaferrite structure. *J. Alloys. Compd.* **2019**, *775*, 1101-8. DOI
25. Pullar, R. C. Hexagonal ferrites: a review of the synthesis, properties and applications of hexaferrite ceramics. *Prog. Mater. Sci.* **2012**, *57*, 1191-334. DOI
26. Ebnabbasi, K.; Mohebbi, M.; Vittoria, C. Room temperature magnetoelectric effects in bulk poly-crystalline materials of M- and Z-type hexaferrites. *J. Appl. Phys.* **2013**, *113*, 17C703. DOI
27. Kitagawa, Y.; Hiraoka, Y.; Honda, T.; Ishikura, T.; Nakamura, H.; Kimura, T. Low-field magnetoelectric effect at room temperature. *Nat. Mater.* **2010**, *9*, 797-802. DOI PubMed
28. Liu, Y.; Wei, T. R.; Wu, J.; et al. Non-layered InSe nanocrystalline bulk materials with ultra-low thermal conductivity. *J. Mater.* **2024**, *10*, 448-55. DOI
29. Al-Hammadi, A. H.; Khoreem, S. H. Investigations on optical and electrical conductivity of Ba/Ni/Zn/$Fe_{16}O_{27}$ Ferrite nanoparticles. *Biointerface. Res. Appl. Chem.* **2022**, *13*, 168. DOI
30. Janu, Y.; Chaudhary, D.; Singhal, N.; et al. Tuning of electromagnetic properties in $Ba(MnZn)_xCo_{2(1-x)}Fe_{16}O_{27}$/NBR flexible composites for wide band microwave absorption in 6-18 GHz. *J. Magn. Magn. Mater.* **2021**, *527*, 167666. DOI
31. Zi, Z. F.; Dai, J. M.; Liu, Q. C.; Liu, H. Y.; Zhu, X. B.; Sun, Y. P. Magnetic and microwave absorption properties of *W*-type $Ba(Zn_xCo_{1-x})_2Fe_{16}O_{27}$ hexaferrite platelets. *J. Appl. Phys.* **2011**, *109*, 07E536. DOI
32. Kresse, G. Ab initio molecular dynamics for liquid metals. *Phys. Rev. B.* **1993**, *192-3*, 222-9. DOI
33. Perdew, J. P.; Burke, K.; Ernzerhof, M. Generalized gradient approximation made simple. *Phys. Rev. Lett.* **1996**, *77*, 3865. DOI PubMed
34. Blöchl, P. E.; Jepsen, O.; Andersen, O. K. Improved tetrahedron method for Brillouin-zone integrations. *Phys. Rev. B. Condens. Matter.* **1994**, *49*, 16223. DOI PubMed
35. Wang, L.; Maxisch, T.; Ceder, G. Oxidation energies of transition metal oxides within the GGA+U framework. *Phys. Rev. B.* **2006**, *73*, 195107. DOI
36. Hill, R. The elastic behaviour of a crystalline aggregate. *Proc. Phys. Soc. A.* **1952**, *65*, 349-54. DOI
37. Momma, K.; Izumi, F. *VESTA 3* for three-dimensional visualization of crystal, volumetric and morphology data. *J. Appl. Crystallog.* **2011**, *44*, 1272-6. DOI
38. Collomb, A.; Wolfers, P.; Obradors, X. Neutron diffraction studies of some hexagonal ferrites: $BaFe_{12}O_{19}$, $BaMg_2$-W and $BaCo_2$-W. *J. Magn. Magn. Mater.* **1986**, *62*, 57-67. DOI
39. Lisjak, D.; Žnidaršič, A.; Sztanislav, A.; Drofenik, M. A two-step synthesis of NiZn-W hexaferrites. *J. Eur. Ceram. Soc.* **2008**, *28*, 2057-62. DOI

40. Yosif, M.; Khan, M. A.; Rasool, R. T.; et al. Impact of Gd-substitution on structural, dielectric, spectroscopic, Raman, and photo luminance properties of $Ba_{0.4}Sr_{0.6}Co_2Fe_{16}O_{27}$ ceramics. *Mater. Chem. Phys.* **2024**, *324*, 129701. DOI
41. Ri, C. H.; Li, L.; Qi, Y. Anisotropy of the electrical conductivity in W-type hexagonal ferrites $BaFe_{18}O_{27}$ and $BaCo_2Fe_{16}O_{27}$ from first principles. *J. Magn. Magn. Mater.* **2012**, *324*, 1498-502. DOI
42. Henkelman, G.; Arnaldsson, A.; Jónsson, H. A fast and robust algorithm for Bader decomposition of charge density. *Comp. Mater. Sci.* **2006**, *36*, 354-60. DOI
43. Kreisel, J.; Lucazeau, G.; Vincent, H. Raman spectra and vibrational analysis of $BaFe_{12}O_{19}$ hexagonal ferrite. *J. Solid. State. Chem.* **1998**, *137*, 127-37. DOI
44. Koide, M.; Kakizaki, K.; Kamishima, K. Synthesis and magnetic properties of Fe_2W and Fe_2Y hexaferrites. *J. Magn. Soc. Jpn.* **2015**, *39*, 147-50. DOI
45. May, A. F.; Snyder, G. J. Introduction to modeling thermoelectric transport at high temperatures. In: Materials, Preparation, and Characterization in Thermoelectrics. New York: CRC Press; 2012. pp. 1-18. DOI
46. Hanus, R.; Agne, M. T.; Rettie, A. J. E.; et al. Lattice softening significantly reduces thermal conductivity and leads to high thermoelectric efficiency. *Adv. Mater.* **2019**, *31*, e1900108. DOI
47. Ma, Y.; Huang, H.; Liu, Y.; et al. Remarkable plasticity and softness of polymorphic InSe van der Waals crystals. *J. Mater.* **2023**, *9*, 709-16. DOI
48. Deng, T.; Wei, T. R.; Huang, H.; et al. Number mismatch between cations and anions as an indicator for low lattice thermal conductivity in chalcogenides. *NPJ. Comput. Mater.* **2020**, *6*, 81. DOI
49. Wu, J.; Lin, Y.; Shu, M.; et al. Uncovering the phonon spectra and lattice dynamics of plastically deformable InSe van der Waals crystals. *Nat. Commun.* **2024**, *15*, 6248. DOI PubMed PMC
50. Lin, J. H.; Hwang, C. S.; Sie, F. R. Preparation and thermoelectric properties of Nd and Dy co-doped $SrTiO_3$ bulk materials. *Mater. Res. Bull.* **2020**, *122*, 110650. DOI
51. Butt, S.; Xu, W.; He, W. Q.; et al. Enhancement of thermoelectric performance in Cd-doped $Ca_3Co_4O_9$ via spin entropy, defect chemistry and phonon scattering. *J. Mater. Chem. A.* **2014**, *2*, 19479-87. DOI
52. Schlichting, K. W.; Padture, N. P.; Klemens, P. G. Thermal conductivity of dense and porous yttria-stabilized zirconia. *J. Mater. Sci.* **2001**, *36*, 3003-10. DOI
53. Callaway, J.; von Baeyer, B. H. C. Effect of point imperfections on lattice thermal conductivity. *Phys. Rev.* **1960**, *120*, 1149. DOI